Correlation between vortex structures and unsteady loads for flapping motion in hover

Thierry Jardin, Ludovic Chatellier, Alain Farcy, Laurent David

▶ **To cite this version:**

Thierry Jardin, Ludovic Chatellier, Alain Farcy, Laurent David. Correlation between vortex structures and unsteady loads for flapping motion in hover. Experiments in Fluids, 2009, vol. 47 (n°4-5), pp. 655-664. 10.1007/s00348-009-0658-x . hal-01132386

HAL Id: hal-01132386
https://hal.science/hal-01132386

Submitted on 17 Mar 2015

HAL is a multi-disciplinary open access archive for the deposit and dissemination of scientific research documents, whether they are published or not. The documents may come from teaching and research institutions in France or abroad, or from public or private research centers.

L'archive ouverte pluridisciplinaire **HAL**, est destinée au dépôt et à la diffusion de documents scientifiques de niveau recherche, publiés ou non, émanant des établissements d'enseignement et de recherche français ou étrangers, des laboratoires publics ou privés.

Open Archive Toulouse Archive Ouverte (OATAO)

OATAO is an open access repository that collects the work of Toulouse researchers and makes it freely available over the web where possible.

This is an author-deposited version published in: http://oatao.univ-toulouse.fr/
Eprints ID: 13655

To link to this article: DOI:10.1007/s00348-009-0658-x
URL: http://dx.doi.org/10.1007/s00348-009-0658-x

To cite this version: Jardin, Thierry and Chatellier, Ludovic and Farcy, Alain and David, Laurent *Correlation between vortex structures and unsteady loads for flapping motion in hover*. (2009) Experiments in Fluids, vol. 47 (n°4-5). pp. 655-664. ISSN 0723-4864

Any correspondence concerning this service should be sent to the repository administrator: staff-oatao@inp-toulouse.fr

Correlation between vortex structures and unsteady loads for flapping motion in hover

Thierry Jardin · Ludovic Chatellier · Alain Farcy · Laurent David

Abstract During the past decade, efforts were made to develop a new generation of unmanned aircrafts, qualified as Micro-Air Vehicles. The particularity of these systems resides in their maximum dimension limited to 15 cm, which, in terms of aerodynamics, corresponds to low Reynolds number flows ($Re \approx 10^2$ to 10^4). At low Reynolds number, the concept of flapping wings seems to be an interesting alternative to the conventional fixed and rotary wings. Despite the fact that this concept may lead to enhanced lift forces and efficiency ratios, it allows hovering coupled with a low-noise generation. Previous studies (Dickinson et al. in Science 284:1954–1960, 1999) revealed that the flow engendered by flapping wings is highly vortical and unsteady, inducing significant temporal variations of the loads experienced by the airfoil. In order to enhance the aerodynamic performance of such flapping wings, it is essential to give further insight into the loads generating mechanisms by correlating the spatial and temporal evolution of the vortical structures together with the time-dependent lift and drag. In this paper, Time Resolved Particle Image Velocimetry is used as a basis to evaluate both unsteady forces and vortical structures generated by an airfoil undergoing complex motion (i.e. asymmetric flapping flight), through the momentum equation approach and a multidimensional wavelet-like vortex parameterization method, respectively. The momentum equation approach relies on the integration of flow variables inside and around a control volume surrounding the airfoil (Noca et al. in J Fluids Struct 11:345–350, 1997; Unal et al. in J Fluids Struct 11:965–971, 1997). Besides the direct link performed between the flow behavior and the force mechanisms, the load characterization is here non-intrusive and specifically convenient for flapping flight studies thanks to its low Reynolds flows' sensitivity and adaptability to moving bodies. Results are supported by a vortex parameterization which evaluates the circulation of the multiple vortices generated in such complex flows. The temporal evolution of the loads matches the flow behavior and hence reveals the preponderant inertial force component and that due to vortical structures.

T. Jardin (✉) · L. Chatellier · A. Farcy · L. David
Laboratoire d'Etudes Aérodynamiques (LEA),
Université de Poitiers, ENSMA, CNRS,
86962 Futuroscope Cedex, France
e-mail: thierry.jardin@lea.ensma.fr

L. David
e-mail: laurent.david@univ-poitiers.fr

1 Introduction

The need for Micro-Air Vehicles (MAVs) to evolve in constraint environments, implying small dimensions and ability to hover, leads to focusing on the aerodynamic performance of flapping wings. Pioneer works (Ellington 1984) based on the flight of insects demonstrate that a wing undergoing flapping motion induces a highly unsteady and vortical flow field responsible for the generation of a strong lifting force. Further numerical and experimental analyses reveal three major phenomena for characterizing this vortical flow field and the resulting lift (Dickinson et al. 1999). (1) As the wing translates at high angle of attack (downstroke and upstroke), a leading edge vortex is formed, inducing a strong suction force on the upper surface (Walker 1931; Dickinson and Götz 1993). This event of significant importance for the aeronautical community (delta wings, helicopter rotor blades) is also referred to as the delayed stall mechanism. (2) At the end of each stroke, as the wing rotates about a spanwise axis (supination and pronation) while still translating, an additional circulation is generated (Kramer 1932; Sane and Dickinson 2002).

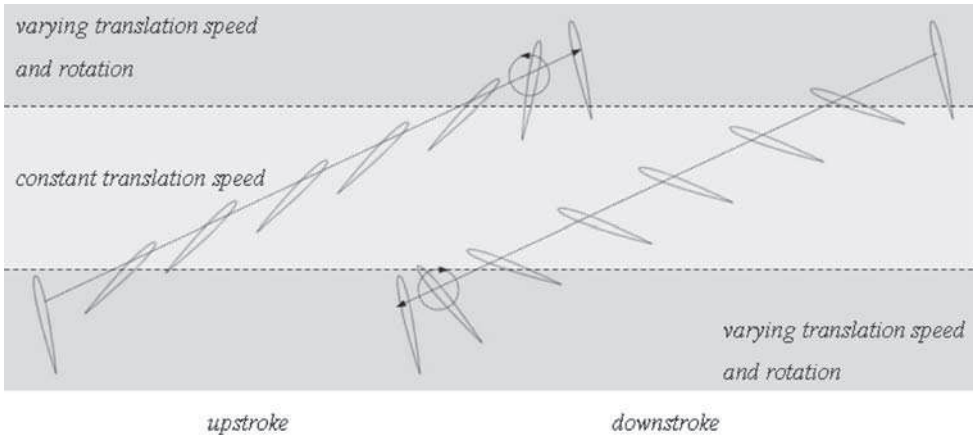

Fig. 1 Description of the asymmetric flapping motion

This phenomenon, known as the Kramer effect, tends to increase lift. (3) As the wing accelerates in the opposite direction to start a new stroke, it encounters the wake generated during the previous stroke (Dickinson 1994). Thus, the force production depends on the positions, dimensions and strengths of the previously shed vortices.

As a consequence, the use of sophisticated experimental tools to correlate the temporal evolution of the vortical structures together with the time-dependent forces experienced by a flapping wing is essential, especially when focusing on the specific configuration of hovering flapping flight (as opposed to forward flapping flight) for which the degree of unsteadiness is maximum. In this paper, an investigation of an asymmetric hovering flapping flight case at Reynolds 1000 (Fig. 1) is carried out by means of TR-PIV measurements which provided a basis to evaluate the unsteady forces acting on and the vortical structures around the airfoil through the momentum equation approach and a multidimensional wavelet-like vortex parameterization method, respectively.

The flapping motion considered is represented in Fig. 1. It is characterized by different upstroke and downstroke angles of attack (20° and 45°, respectively), which implies an inclined stroke plane in order to maintain hovering, i.e. a zero mean horizontal force over a flapping period. A particular interest of such asymmetric motions resides in the fact that the vertical aerodynamic force is hence a combination of both lift and drag (Wang 2004). Furthermore, the main aerodynamic mechanisms significantly differ from the ones observed in symmetric or "normal" hovering flapping flight (a complementary study of normal hovering may be found in Kurtulus et al. 2008).

2 Unsteady loads evaluation

The evaluation of two-dimensional loads is deduced from the TR-PIV measurements. The method is based on the integration of flow variables inside and around a control volume surrounding the airfoil (Noca et al. 1997, 1999; Unal et al. 1997). Besides the fact that the loads characterization is here non-intrusive, the approach is particularly powerful in the sense that it allows a direct link between flow behavior and force mechanisms, which is not a priori the case when separate techniques are used to extract these informations. Moreover, the inherent characteristic of a non-intrusive method is to remove the necessity of model instrumentation (e.g. pressure probes) so that the approach may be qualified as cost-effective. In the recent context of flapping flight investigation, and more generally of MAVs development, the method furthermore appears as specifically convenient thanks to its sensitivity to low Reynolds flows and its adaptability to moving bodies. For such cases, the use of piezo-electric gauges introduces non-negligible relative errors caused by the range of measures (e.g. 10 g loads) as well as the presence of an inertial component (for non-constant motion).

The approach may be considered under distinguished forms. Lin and Rockwell (1996) apply a variant based on the knowledge of the entire vorticity field surrounding a body (impulse concept, Lighthill 1986) to an oscillating cylinder in quiescent water. Conducting similar experiments, Noca et al. (1997) extend the approach for a finite volume of control. The particularity of the formulation resides in the absence of a pressure term, eliminated from the momentum equation by algebraic manipulations. Protas et al. (2000) successfully implement their numerical computations with Quartapelle and Napolitano (1982) equation in which the pressure term is also eliminated giving rise to a new flow-independent but geometry-dependent variable. Unal et al. (1997) suggests another variant for minimizing the evaluation of spatial derivatives where the pressure term is deduced from the integration of the pressure gradient. Its application on an oscillating cylinder at Reynolds 3780 shows correct agreement with the forces obtained by means of both a transducer and the circulation theorem.

An identical approach is recently performed to evaluate the unsteady aerodynamic forces acting on a fixed square cross-sectional cylinder at a Reynolds number of 4900 (Kurtulus et al. 2007). The variant is also applied to a steady supersonic flow around a bi-convex airfoil (Oudheusden et al. 2007). Note that a parametrical comparison between distinguished forms may be found in Noca et al. (1999).

The present study is based on the application of the momentum equation approach to the highly vortical and unsteady flow fields determined by TR-PIV for a two-dimensional moving profile undergoing complex motion, i.e. asymmetric hovering flapping flight.

2.1 Theory

Equation (1) gives the instantaneous force $\vec{F}(t)$ experienced by the airfoil as function of four components:

$$\vec{F}(t) = -\rho \iiint_V \frac{\partial \vec{V}}{\partial t} \mathrm{d}V - \rho \iint_S (\vec{V} \cdot \vec{n})(\vec{V} - \vec{V}_s)\, \mathrm{d}S - \iint_S p\vec{n}\, \mathrm{d}S + \iint_S \bar{\bar{\tau}}\, \vec{n}\, \mathrm{d}S \quad (1)$$

where $\vec{n}$ is the normal to the control surface S limiting the control volume V as shown in Fig. 2, ρ the fluid density, $\vec{V}$ the flow velocity vector, $\vec{V}_S$ the velocity of the control volume and $\bar{\bar{\tau}}$ the viscous stress tensor.

The unsteady and convective terms (the first two right-hand side contributions) are directly deduced from the TR-PIV velocity flow fields and account for the rate of change of momentum due to the flow unsteadiness within the control volume and the convection across the control surface, respectively. Note that the convective term is not integrated over the airfoil surface since $(\vec{V} - \vec{V_s})$ equals zero for a no-through flow boundary condition. The third term represents the normal stresses acting on the control surface. Its deduction requires the knowledge of the pressure p, obtained through the integration of the pressure gradient along the control surface. The pressure gradient is calculated from the momentum equation:

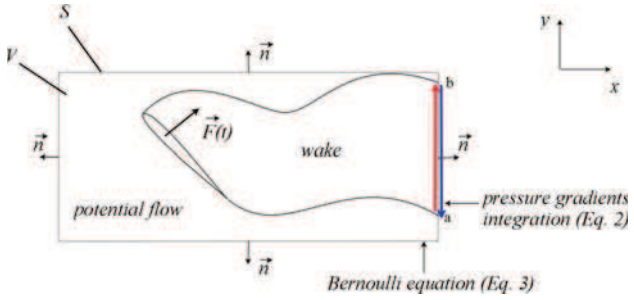

Fig. 2 Control volume definition and pressure evaluation process

$$\frac{\mathrm{D}\vec{V}}{\mathrm{D}t} = -\frac{1}{\rho}\nabla p + \nu \nabla^2 \vec{V} \quad (2)$$

The last term accounts for the viscous stresses on the control surface. It is derived from the velocity flow fields but may be neglected for preponderant pressure force flows or if the control surface is sufficiently far away from the airfoil. In our case, it contributes to 0.1% of the lift and drag magnitude.

The present experiments are performed on a two-dimensional airfoil so that the calculation of Eq. (1) is reduced to the integration of the flow variables inside a two-dimensional domain. The x and y aerodynamic coefficients C_d and C_l are deduced from the adimensionalization of the x and y components F_d and F_l of the unsteady force $\vec{F}(t)$ using the constant translation speed V_0 reached during downstroke and upstroke and the chord of the airfoil c such that $C_d = \frac{2F_d}{\rho c V_0^2}$ and $C_l = \frac{2F_l}{\rho c V_0^2}$. Note that x is collinear to the stroke plane and thus depends on the asymmetry of the motion.

2.2 Solution methods

The spatial and temporal derivations of the velocity vectors and the spatial integrations along the control surface and in the control volume are achieved using second order central finite difference numerical schemes and the Simpson formula, respectively.

The value of Δt for the calculation of the acceleration may be chosen to reduce the influence of the experimental uncertainties without significantly affecting the effective level of acceleration (David et al. 2006). Nevertheless, in order to limit the temporal oscillations (due to the experimental uncertainties) of the unsteady loads obtained through Eq. (1), PIV data are smoothed using sliding fifth order temporal polynomials, determined by a least square method in the interval $[t - \frac{t^*}{4}; t + \frac{t^*}{4}]$, so that Δt is set to $0.08t^*$, where $t^* = c/V_0$.

As previously expressed, the pressure p in Eq. (1) is deduced from the second order integration of the pressure gradient along the control surface. When the present approach is applied to experimental flow fields, i.e. subjected to measurement uncertainties, this integration step induces an effect of error propagation. In other words, the measurement error committed on a velocity vector is transmitted to the pressure gradient (Eq. 2) and propagated along the control surface through the integration of the latter. In order to minimize this effect and to increase the consistency of the pressure evaluation, the flow is considered as potential in regions where the vorticity may be considered as negligible, i.e. its magnitude is below a specified threshold. As a consequence, either the Bernoulli equation or the integration of the pressure gradients is used

whether the flow may or may not be considered as potential (Fig. 2). Furthermore, the error linked to the propagation phenomenon increases with the number of integration steps. Thus, in vortical regions, it is convenient to evaluate the pressure as the weighted value of the pressures deduced by integrating the pressure gradients both clockwise and counter-clockwise. Nevertheless, for two-dimensional quality measurements, the error propagation is weak. In our case, we estimated that fixing the nondimensional vorticity threshold to 0.1, which is two orders of magnitude below the typical vorticity levels of the flow, only reduces by 1% the error committed on the pressure term. The pressure evaluation stands as a critical point in the process of load prediction since the spatial derivatives used to calculate the pressure gradients in Eq. (2) emphasize the experimental uncertainties. Note that extending this evaluation to the entire flow domain either through the integration of the pressure gradients or by means of the Poisson equation is currently under much consideration (Kat et al. 2008).

The resolution has been validated and a parametrical study has been carried out (dimensions and positions of the control volume, vorticity threshold, presence of a spanwise component, numerical schemes, time step) using numerical flow fields obtained by directly solving the Navier–Stokes equations (DNS) on an impulsively started NACA0012 profile (Jardin et al. 2008; David et al. 2009). In particular, the two-dimensional approach applied on three-dimensional flow fields demonstrated that the presence of a spanwise velocity component significantly affect the accuracy of the results. Furthermore, the introduction of a random noise reaching a maximum of ±10% of the velocity vectors intensity induces a mean error on the unsteady, convective and pressure contributions of 2, 3.5, 11% and 0.5, 0.5, 6% for the drag and lift predictions, respectively.

3 Vortex parameterization

The vortical activity in a given flow field can be characterized by a number of indicators, such as vorticity, enstrophy (Schram et al. 2004), Γ_2 (Michard and Favelier 2004), or the three topological quantities: Q factor (Chong et al. 1990), λ_2 (Jeong and Hussain 1995) and d_2 (Vollmers 2001), which are equivalent in the case of two-dimensional incompressible flows.

Jeong and Hussain's λ_2 criterion is being increasingly used for its detection performances in both two- and three-dimensional incompressible flows, although the general discussion remains open (see Haller 2005 for example). Because a generalization of the present method to three-dimensional λ_2 distributions appears possible, the λ_2 notation will be used here. Essentially, Jeong and Hussain have demonstrated that, in favorable conditions, regions in which the second highest eigenvalue of the tensor $\Omega^2 + S^2$, λ_2, is negative, indicate the extent of a zone of vortical activity, say, a vortex. In a two-dimensional flow, λ_2 is expressed as follows:

$$\lambda_2 = \frac{\partial u}{\partial y}\frac{\partial v}{\partial x} - \frac{\partial u}{\partial x}\frac{\partial v}{\partial y} \tag{3}$$

which yields, in polar coordinates and in the case of a purely tangential motion ($v_r = 0$ and $v_\theta(r)$):

$$\lambda_2 = -\frac{v_\theta}{r}\frac{\partial v_\theta}{\partial r} \tag{4}$$

Among this type of flows, the Oseen vortex of circular section is an instantaneous solution of the Navier-Stokes equation, and is defined by:

$$v_r(r) = 0 \tag{5}$$

$$v_\theta(r) = \frac{\Gamma}{2\pi r}\left(1 - e^{r^2/r_0^2}\right) \tag{6}$$

where Γ and r_0 are the vortex circulation and core radius, respectively. The corresponding λ_2^0 distribution is then:

$$\lambda_2^0(r) = \frac{\Gamma^2}{4\pi^2 r^2}\left[\frac{1}{r^2} - \left(\frac{1}{r^2} + \frac{2}{r_0^2}\right)e^{r^2/r_0^2}\right]\left(1 - e^{r^2/r_0^2}\right) \tag{7}$$

An interesting property of this theoretical formulation is that it satisfies the initial definition of a wavelet, as it is zero-mean and square integrable.

Continuous wavelets have been used in a number of studies in order to extract and parameterize circular-section vortices according to their alikeness to the Oseen vortex. Most authors have used the so-called Mexican hat wavelet to compute wavelet transforms of λ_2 (Anthoine et al. 2003), enstrophy (Schram et al. 2004) or d_2 distributions (Varun et al. 2008). In parallel, a calibration of the wavelet transform against the theoretical Oseen model allows the estimation of the scale and intensity of candidate vortices. In all these methods, the mother wavelet is used as an intermediary parameterizing function between the experimental field and the model. Here, a mother wavelet based on Eq. (7) is used, so that a direct parameterization of a candidate vortex against the model is possible. In practice, once local maxima of the wavelet coefficient resulting from the wavelet transform of λ_2 are found, the radii of the corresponding Oseen vortices are directly known and their circulation is proportional to the square root of the wavelet coefficient.

Additionally, the use of a model-based wavelet allows the introduction of multiple parameters, which conserve their physical meaning in the process of a wavelet transform. Although the full geometry of an actual vortex may not be given by a simple synthetic model, parameters such as ellipticity, orientation, radial deformation, etc. can

be introduced in order to enhance the accuracy of the detection and parameterization algorithm.

Here, the mother wavelet is based on the normalized λ_2 distribution obtained from the elliptic-section Oseen vortex, which can be deduced from the circular-section vortex case via linear transformations. The mother wavelet is then defined by its scale, translation, ellipticity and orientation parameters.

Given experimental λ_2 distributions, a multi-parameter analysis of the wavelet coefficients is carried out through a multi-dimensional optimization algorithm based on the Nelder and Mead's simplex technique (Nelder and Mead 1965). This kind of algorithm does not fully scan all the dimensions of parameterization, as in a conventional wavelet transform, but follows multi-dimensional paths leading to local maxima of the wavelet coefficient.

Using this approach, the present procedure allows direct parameterization of the identified elliptic vortices in terms of position, scale, ellipticity and orientation. Once the identification of these parameters is obtained, the circulation of each vortex is directly deduced from the wavelet coefficient associated with the optimized parameters.

Figure 3 illustrates the capacity of parameterization of the method. The position and a first estimation of the scale and circulation of candidate vortices are initially given by a conventional wavelet transform based on the circular model. Some candidate vortices are rejected if they do not satisfy a threshold based on the standard deviation of the λ_2 distribution and if the flow does not locally exhibit a coherent rotation pattern. Then, ellipticity, orientation, refined scale and circulation are obtained from the optimization algorithm. Additionally, vortices detected too close to a boundary or intricate vortices are rejected; the minimum acceptable separation distance between two vortices is set to the sum of their radii.

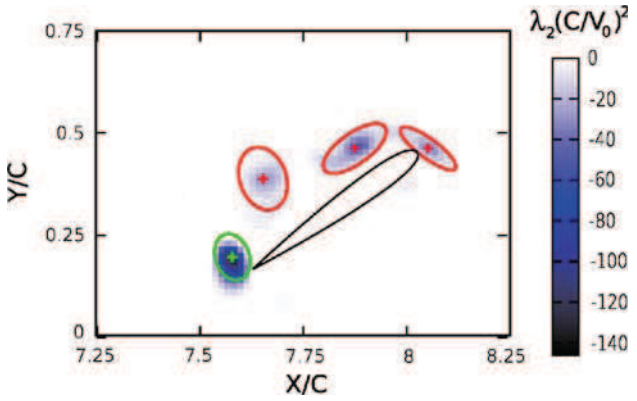

Fig. 3 Zoomed view of the λ_2 distribution around the airfoil at $t/T = 0.45$. The detected vortices are indicated as *red* (positive circulation) and *green* (negative circulation) ellipses at model scale

On synthetic velocity fields containing only elliptical Oseen vortices, the algorithm can achieve the estimation of the parameters with a relative precision depending mainly on the scale and ellipticity parameters. Essentially, the relative accuracy is degraded for large ellipticity and scale parameters, but remains below 1% for radii comprised between 1 and 5 grid cells and for an ellipticity parameter lower than 4. For radii inferior to the PIV cell size, the global accuracy is of the same order, but erratic results may appear, as the sub-grid localization is made difficult by the very compact support of the wavelet. Consequently, identification of the smallest structures must be conducted with care.

In terms of robustness to noise, tests on synthetic velocity fields polluted with Gaussian random noise have revealed that the loss of accuracy is of the order of the noise-to-maximum velocity ratio. The analysis of the present experimental results has shown that the difference between the initial velocity fields and the velocity fields locally reconstructed from the identified vortices is, on average, of the order of 10% of the maximum velocity of the model vortex. Consequently, the circulation-based lift predictions will be obtained with a corresponding accuracy.

4 Experimental setup

The experiments are conducted in a $1 \times 1 \times 2$ m^3 water tank filled with 15 μm diameter hollow silver coated glass particles. The airfoil is a transparent resin NACA0012 profile connected at both ends to Plexiglas plates which limit three-dimensional effects. The chord and wingspan are, respectively, 60 and 500 mm long. The translational and rotational motions of the airfoil are driven separately through the use of two servo-controlled motors. Their respective mechanical transmissions are achieved by means of an endless screw and a pulley as shown in Fig. 4.

TR-PIV is performed with two JAI 8-bits cameras taking images every 1/1,000 period during the seventh period of the flapping motion, for which the flow is ensured to be periodical. The time step allows an accurate calculation of both velocity and acceleration flow fields. Each camera is equipped with a 50 mm focal length lens, $F_{\#}$ 2.8, for a 370×280 mm^2 area imaging. The laser sheet, in the airfoil mid-span plane, is provided directly and indirectly (through the use of an optical fiber) by a continuous 4.5 W argon laser system (Fig. 4). The light is equally shared to illuminate both sides of the airfoil. This method is adopted in order to reduce the shadow effects.

The velocity flow fields for each camera are deduced from the TR-PIV images using the 7.2 LaVision software. A multipass algorithm with a final interrogation window size of 16×16 pixels and 50% overlapping is applied.

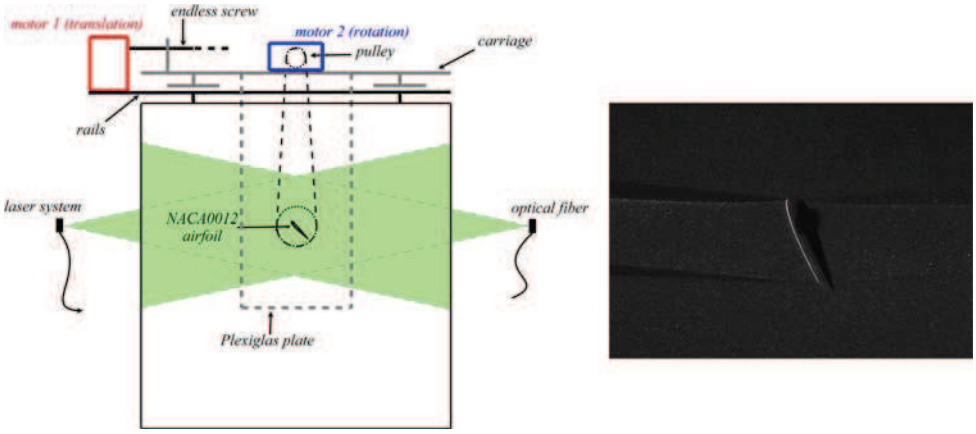

Fig. 4 Experimental setup and an example of PIV images

Image deformation and round Gaussian weighting function are used. Spurious velocities are identified and replaced with a median filter.

The final velocity flow fields are reconstructed using Kriging interpolation from the combination of both cameras' information and known boundary conditions on the airfoil surface. The advantages of using two cameras are (1) to increase the spatial resolution and (2) to avoid inaccessible regions due to the perspective effect. The cameras share a common view zone so that the velocity flow fields on the left and right side of the profile come from the left and right cameras, respectively. The final flow fields have an area of 570×280 mm^2.

5 Results

TR-PIV measurements allow determination of the vorticity fields generated by the profile undergoing asymmetric flapping motion of period T and hence provide evidence of the spatial and temporal evolution of the vortical structures. This evolution is correlated with the unsteady lift and drag forces obtained through the use of the momentum equation approach applied to the TR-PIV velocity fields as well as the lift force found by the circulation theorem.

5.1 Wake analysis

Figure 5 displays the non-dimensional vorticity flow fields at different instants during the flapping motion. One should have in mind that the translation is taking place along an inclined path.

At $t/T = 0$, the airfoil is rotating about its spanwise axis located 1/4 chord away from the leading edge. The flow is characterized by two main clockwise (LEV1) and counter-clockwise (TEV1) rotating structures corresponding to the shedding of the Leading Edge Vortex and the attachment of the Trailing Edge Vortex formed during the previous stroke. Secondary structures observed as negative vorticity spots in the vicinity of the profile (LEV2) result from the interaction of a second nascent Leading Edge Vortex, formed during the latter part of the previous stroke, with the Trailing Edge Vortex (TEV1).

At $t/T = 0.05$, the airfoil is translating while still rotating to reach a 20° angle of attack. The rotating motion influences the unsteady behavior of the flow (1) by delaying the formation of the Starting Vortex (SV1) and (2) by supporting the formation of a new Leading Edge Vortex (LEV3). The latter is furthermore strengthened by the presence of a fluid jet directed towards the airfoil by the combined action of LEV1 and TEV1 as shown in Fig. 5. At $t/T = 0.15$, the interaction of the airfoil with LEV1 leads to the shedding of LEV3. As the translating motion is maintained, one can notice that the flow remains attached to the airfoil in contrast to the fact that the angle of attack is fixed to 20°, which is above the critical stall incidence for a NACA0012 profile. This observation is attributable to the presence of a fluid downwash, resulting from the lift generation of the previous strokes, which tends to decrease the effective angle of attack. Nevertheless, the latter strongly depends on the environing conditions (e.g. previous strokes' vorticity) and hence appears as particularly unstable such that a weak Leading Edge Vortex (LEV4) is finally formed at the end of upstroke.

At $t/T = 0.5$, the airfoil is subjected to the opposite motion to that experienced at $t/T = 0$. However, the flow behavior is fundamentally different since no Leading Edge Vortex was shed during upstroke. The direct consequence resides in the absence of significant wake capture during downstroke: as the airfoil starts the downstroke translation, LEV4 slides on the lower surface to the trailing edge, supporting the formation of a new Starting Vortex (SV2) without affecting the nascent Leading Edge Vortex (LEV5). The latter is hence growing smoothly to form a consequent low-pressure region on the upper surface at

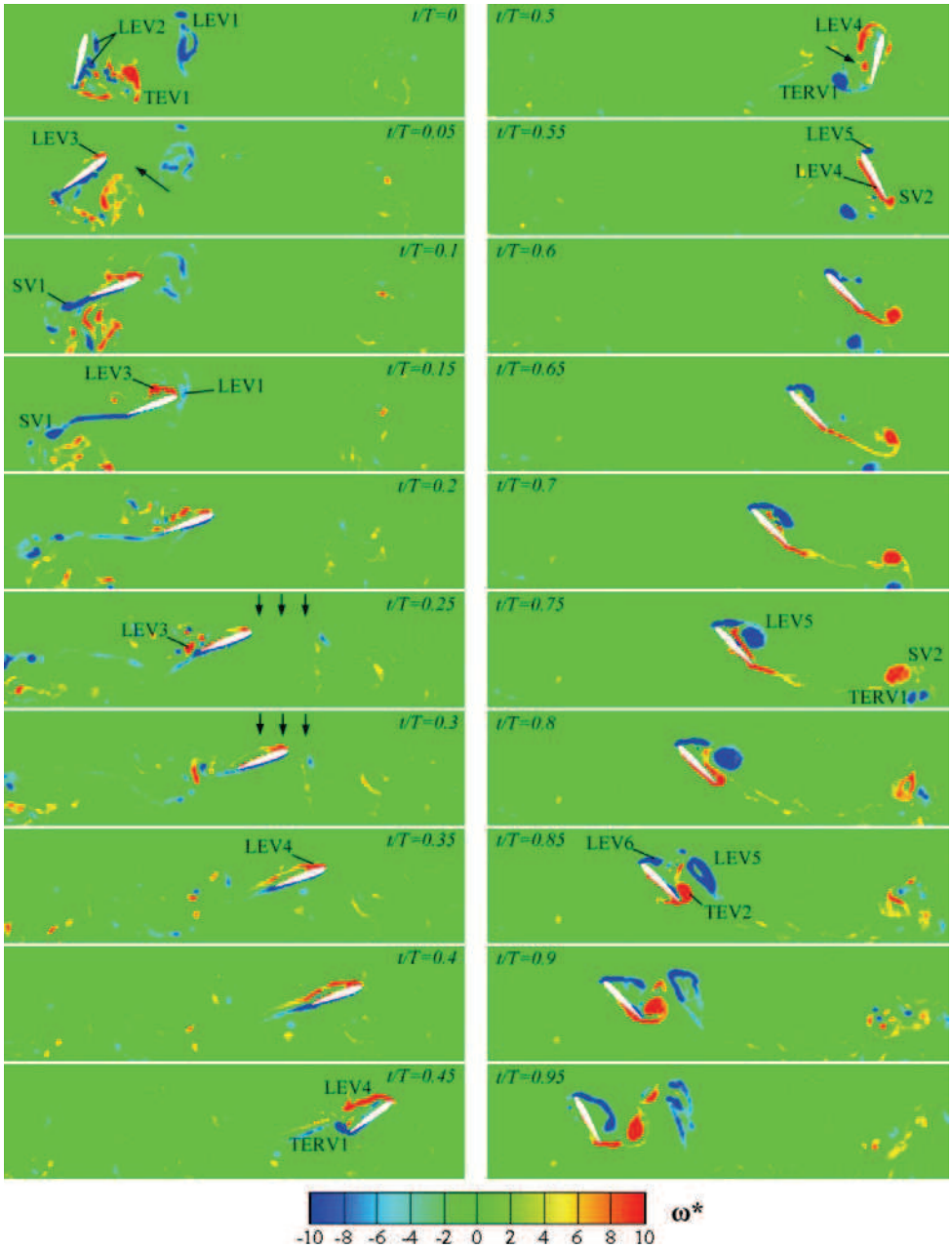

Fig. 5 Non-dimensional vorticity fields and main vortical structures (upstroke *left*, downstroke *right*)

$t/T = 0.75$. Its influence on the generation of lift is enhanced as compared to that of a LEV affected by the wake. In parallel, TERV1 (Trailing Edge Vortex formed by the rotating motion) and SV2 join to form a vortex dipole.

At $t/T = 0.85$, the vortex dipole collapses and LEV5 is shed into the wake. With the presence of the Trailing Edge Vortex TEV2 and the formation of a new Leading Edge Vortex LEV6, the flow field tends to reach a von Karman shedding state. Note that LEV5, LEV6 and TEV2 may be considered as LEV1, LEV2 and TEV1, respectively, putting into evidence the periodical aspect of the flow.

5.2 Resulting loads

The wake analysis reveals the presence of multiple vortices whose spatial and temporal characteristics directly affect the temporal evolution of the unsteady aerodynamic coefficients displayed in Fig. 6. The evolution of the unsteady loads may be separated into distinguished components corresponding to the preponderant inertial (rotation and varying speed translation) motion and that due to the evolution of the vortical structures during constant translation motion. The representation of the respective unsteady, convective and pressure contributions, allows further insight into the force generating mechanisms.

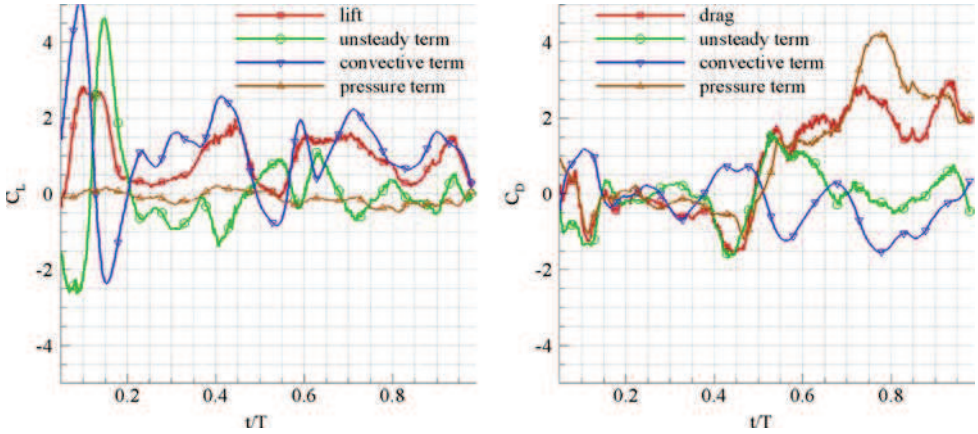

Fig. 6 Unsteady lift and drag coefficients and the respective unsteady, convective and pressure contributions

Prior to the analysis of the lift and drag temporal evolutions, it is important to note that the pressure contribution is quasi null for the lift prediction but preponderant for the drag prediction. Considering the previous remarks suggested in Sect. 2.2, it is hence probable that evaluating the drag by means of the momentum equation is less accurate than evaluating the lift. Furthermore, the latter is supported by the circulation theorem approach which shows correct agreement in regions where the effects of added mass (not taken into account when summing the vortex circulations) are absent (Fig. 7). We remind that according to the potential flow theory, an estimation of the instantaneous lift coefficient can be obtained from the circulation of all the identified vortices, through the expression $C_l = \frac{2\Gamma}{cV_0}$. Better comparison could still be achieved by restricting the approach to long life/strong vortices, reducing the background noise.

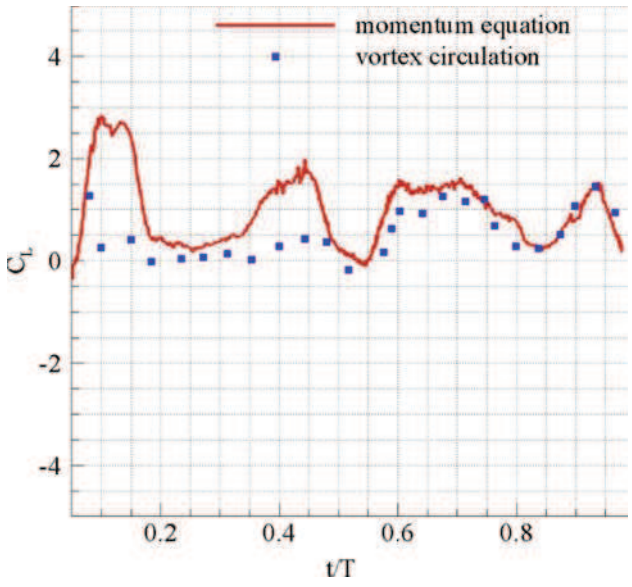

Fig. 7 Comparison of lift coefficients calculated via the momentum equation and the circulation theorem

5.2.1 *Lift prediction*

The first event represented in Fig. 6 is a strong positive peak of the lift from $t/T = 0.1$ to $t/T = 0.15$ induced by the growth of LEV3 as the airfoil translates through its wake. The shedding of LEV3 due to its interaction with LEV1 implies a sharp decrease of the lift which tends to a weak value ($C_l \approx 0.5$). The lift remains constant between $t/T = 0.2$ and $t/\mathrm{T} = 0.325$ until the formation of LEV4.

From $t/T = 0.4$, the influence of LEV4 on lift enhancement is superimposed with both rotating and decelerating inertial effects. Furthermore, this influence depends on the relative positions of LEV4 and the airfoil, hence varying according to the angle of attack variation. As a consequence, the lift coefficient increases to approximately 1.5 at $t/T = 0.45$ before sharply tending to zero at the end of upstroke.

At $t/T = 0.5$, the unsteady lift exhibits a quasi-null value due to the position of the airfoil (i.e. nearly vertical) as well as a zero translation speed. The following acceleration coupled with a decreasing angle of attack leads to the rapid increase of the lift through both the inertial effects and the formation of LEV5. This increase seems reduced slightly after $t/T = 0.6$ which matches the end of the rotation and varying translation speed phase, hence the contribution of the inertial forces. Note that latency probably arising from viscous effects is observed between the end of the rotation and varying translation speed phase ($t/T = 0.61$) and the effective influence of the inertial forces on the unsteady lift ($t/T \approx 0.62$).

The spatial and temporal behavior of LEV5 guides the temporal evolution of the lift throughout the constant speed translation phase. Thus, a substantial level of lift ($C_l \approx 1.5$) is maintained when LEV5 is closely attached to the airfoil, followed by a decrease (from $t/T = 0.73$) as LEV5 smoothly detaches to be shed into the wake. The unsteady lift reaches its lowest value ($C_l \approx 0.45$) near

$t/T = 0.85$ and is then subjected to the influence of LEV6 as evident by its consequent increase.

At $t/T = 0.9$, besides the decrease in translation speed, the previous lift enhancement seems maintained, and eventually strengthened, through the rotating motion which adds supplementary circulation to the environing fluid. As the airfoil angle of attack is such that LEV6 is less effective, the lift tends sharply to a zero value.

5.2.2 Drag prediction

On the contrary to the lift coefficient, the pressure contribution (for which arises the major errors due to experimental uncertainties) of the drag coefficient may not be considered as negligible. Thus, the analysis of the drag temporal evolution should be treated with great care, specifically when strong variations of the pressure contribution are exhibited.

In this section, for sake of clarity, we remind that the x component of the force $\vec{F}(t)$acts as drag when it is negative/positive during upstroke/downstroke and as thrust when it is positive/negative during upstroke/downstroke.

At $t/T = 0.12$, the drag exhibits a negative peak probably arising from the translating acceleration combined with the formation of LEV3. Between, $t/T = 0.2$ and $t/T = 0.4$, the drag is weak, quasi unaffected by the presence of LEV3 (shed in the wake through the wake capture) and LEV4, the airfoil position being parameterized with a low angle of attack. A significant augmentation is observed at $t/T = 0.4$ as the airfoil starts to rotate, increasing its angle of attack, hence its y axis projected surface. The latter effect is combined with a dropping translation speed such that the drag reaches its maximum value at $t/T = 0.45$ and rapidly decreases until the end of upstroke. It is here clear that the corresponding phase is dominated by the inertial effects.

At the beginning of downstroke, the relative positions of LEV4 and TERV1 induce a fluid jet oriented towards the airfoil surface (Fig. 5) which supports the production of drag. As LEV4 slides on the lower surface ($t/T \approx 0.55$), the augmentation of drag by the fluid jet is eliminated. However, as observed for the lift, a substantial level due to the attachment of LEV5 on the airfoil surface is maintained throughout the downstroke. At $t/T = 0.75$, the drag decreases along with the shedding of LEV5 but is rapidly enhanced by the formations of TEV2 and LEV6.

6 Conclusion

Time Resolved Particle Image Velocimetry is used as a basis to evaluate both (1) the spatial and temporal evolution of the vortical structures generated around a two-dimensional NACA0012 airfoil undergoing asymmetric flapping motion and (2) the resulting unsteady lift and drag through the momentum equation approach and a multidimensional wavelet-like parameterization. The latter, based on the λ_2 distribution, demonstrates correct agreement with the momentum equation approach when predicting the lift in regions where inertial forces are not preponderant. Hence, the use of both methods allows an accurate temporal correlation and further insight into the lift generating mechanisms, which is essential when focusing on aerodynamic performance enhancement. Despite the complex motion of the airfoil involving the contribution of strong inertial force components and generation of highly unsteady vortical flow fields, the lift and drag exhibit levels and temporal behavior consistent with the dimensions, formations and shedding of the multiple vortices. In particular, it is shown that the aerodynamic forces principally arise from (1) the presence of Leading Edge Vortices during the constant translation speed phases, (2) the inertial force components during the rotating and varying translation speed phases and (3) the relative positions of the shed vortices which may in some cases induce significant fluid jets impacting the airfoil. Note that these observations augment the description of the mechanisms mentioned in the introduction. Nevertheless, one should keep in mind that, on the contrary to the lift evaluation, the drag prediction by means of the momentum equation approach is subjected to specific difficulties linked to the pressure contribution evaluation.

References

Anthoine J, Mettenleiter M, Repellin O, Buchlin J-M, Candel S (2003) Influence of adaptive control on vortex-driven instabilities in a scaled model of solid propellant motors. J Sound Vib 262:1009–1046

Chong MS, Perry AE, Cantwell BJ (1990) A general classification of three-dimensional flow field. Phys Fluids A 2:765–777

David L, Scarano F, Braud P (2006) Accéléromètrie plane par PIV-TR ou double plans: avantages et limitations. 10ème Congrès Francophone de Techniques Laser, Toulouse, France

David L, Jardin T, Farcy A (2009) Validation of unsteady lift and drag evaluation by TR-PIV. Meas Sci Technol (submitted)

Dickinson MH (1994) The effects of wing rotation on unsteady aerodynamic performance at low Reynolds number. J Exp Biol 192:179–206

Dickinson MH, Götz KG (1993) Unsteady aerodynamic performance of model wings at low Reynolds number. J Exp Biol 174:45–64

Dickinson MH, Lehmann FO, Sane SP (1999) Wing rotation and the aerodynamic basis of insect flight. Science 284:1954–1960

Ellington CP (1984) The aerodynamics of hovering insect flight. Phil Trans R Soc Lond 305:1–181

Haller G (2005) An objective definition of a vortex. J Fluid Mech 525:1–26

Jardin T, David L, Farcy A (2008) Unsteady flow diagnostics for hovering flapping flight. EWA international workshop, advanced measurement techniques in aerodynamics, Delft, Netherlands, 31-1 April 2008

Jeong J, Hussain F (1995) On the identification of a vortex. J Fluid Mech 285:69–94

Kat R, Oudheusden BW, Scarano F (2008) Instantaneous planar pressure field determination based on time-resolved Stereo-PIV. EWA international workshop, advanced measurement techniques in aerodynamics, Delft, Netherlands, 31-1 April 2008

Kramer M (1932) Die Zunahme des Maximalauftriebes von Tragflugeln bei plotzlicher Anstellwinkelvergrosserung. Z Flugtech Motorluftschiff 23:185–189

Kurtulus DF, Scarano F, David L (2007) Unsteady aerodynamic forces estimation on a square cylinder by TR-PIV. Exp Fluids 42:186–196

Kurtulus DF, David L, Farcy A, Alemdaroglu N (2008) Aerodynamic characteristics of flapping motion in hover. Exp Fluids 44:23–36

Lighthill J (1986) Fundamentals concerning wave loading on offshore structures. J Fluid Mech 173:667–681

Lin JC, Rockwell D (1996) Force identification by vorticity fields: techniques based on flow imaging. J Fluids Struct 10:663–668

Michard M, Favelier T (2004) Développement d'un critère d'identification de structures tourbillonnaires adapté aux mesures de vitesse par PIV. 9ème Congrès Francophone de Vélocimétrie Laser, Bruxelles, Belgium

Nelder JA, Mead R (1965) A simplex method for function minimization. Comput J 7:308–313

Noca F, Shiels D, Jeon D (1997) Measuring instantaneous fluid dynamic forces on bodies, using only velocity fields and their derivatives. J Fluids Struct 11:345–350

Noca F, Shiels D, Jeon D (1999) A comparison of methods for evaluating time-dependent fluid dynamic forces on bodies, using only velocity fields and their derivatives. J Fluids Struct 13: 551–578

Oudheusden BW, Scarano F, Roosenboom EWM, Casimiri EWF, Souverein LJ (2007) Evaluation of integral forces and pressure fields from planar velocimetry data for incompressible and compressible flows. Exp Fluids 43:153–162

Protas B, Styczek A, Nowakowski A (2000) An effective approach to computation of forces in viscous incompressible flows. J Comput Phys 159:231–245

Quartapelle L, Napolitano M (1982) Force and moment in incompressible flows. AIAA J 21:911–913

Sane SP, Dickinson MH (2002) The aerodynamic effects of wing rotation and a revised quasi-steady model of flapping flight. J Exp Biol 205:1087–1096

Schram C, Rambaud P, Riethmuller ML (2004) Wavelet based eddy structure eduction from a backward facing step flow investigated using particle image velocimetry. Exp Fluids 36:233–245

Unal MF, Lin JC, Rockwell D (1997) Force prediction by PIV imaging: a momentum-based approach. J Fluids Struct 11:965–971

Varun AV, Balasubramanian K, Sujith RI (2008). An automated vortex detection scheme using the wavelet transform of the d_2 field. Exp Fluids (online)

Vollmers H (2001) Detection of vortices and quantitative evaluation of their main parameters from experimental velocity data. Meas Sci Technol 12:1199–1207

Walker PB (1931) Growth of circulation about a wing and an apparatus for measuring fluid motion. ARC report

Wang ZJ (2004) The role of drag in insect hovering. J Exp Biol 207:4147–4155